CHEMISTRY OF MATERIALS

ARTICLE

pubs.acs.org/cm

Spectroscopic Investigation of Ti-Modified Aluminum-Free Zeolite-Beta Crystallization

Mojca Rangus,[†] Matjaž Mazaj,[†] Iztok Arčon,[‡,§] Gregor Mali,[*,†,⊥] and Venčeslav Kaučič[†]

[†]National Institute of Chemistry, Hajdrihova 19, SI-1001 Ljubljana, Slovenia

[‡]Institute Jožef Stefan, Jamova 39, SI-1000 Ljubljana, Slovenia

[§]University of Nova Gorica, Vipavska 13, SI-5000 Nova Gorica, Slovenia

[⊥]EN→FIST Centre of Excellence, Dunajska 156, SI-1000 Ljubljana, Slovenia

Supporting Information

ABSTRACT: Crystallization of aluminum-free zeolite-Beta from viscous gel and incorporation of titanium into its framework were investigated by several spectroscopic techniques. Hydrothermal synthesis was stopped at different times and the gels obtained from the autoclaves were analyzed by liquid-state ^{29}Si NMR spectroscopy. The gels were subsequently dried and inspected by solid-state ^{29}Si NMR, Fourier-transform infrared, and X-ray absorption spectroscopy. NMR spectroscopy distinguished signals from oligomers and from two populations of nanoparticles with different typical dimensions. It also provided information about the composition of the oligomers and nanoparticles, in terms of the relative fractions of Q^n units within them. Investigation showed that the synthesis of zeolite Ti-Beta started with a quick formation of oligomers. After 20 h of the hydrothermal treatment, oligomers with a high fraction of Q^3 units gradually aggregated into primary nanoparticles with a diameter of ~2 nm. During first 20 h, primary nanoparticles began to agglomerate into secondary nanoparticles with a diameter of 5−10 nm. These nanoparticles already had a high fraction of Q^4 units and already possessed a zeolitic character. With a further increase in the hydrothermal treatment time, the concentration of secondary nanoparticles increased and they started to gather into zeolitic crystallites. Ti atoms were incorporated into the growing silicate framework at a very early stage of the crystallization process.

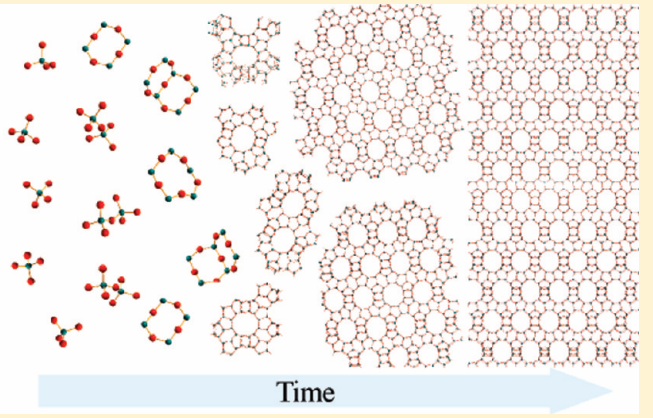

KEYWORDS: porous materials, nanomaterials, crystal growth

INTRODUCTION

Nanosized zeolites with crystallite dimensions below 100 nm have attracted considerable attention, because of the increased external surface values and surface energies and decreased channel lengths, compared to the conventional micrometer-sized zeolite crystals.[1,2] The catalytic sites due to the incorporated aluminum (Lewis and Brønsted acid sites) or transition-metal atoms (redox and oxidation sites) are, in nanosized zeolites, more easily accessible; therefore, such zeolites exhibit high catalytic efficiencies in many catalytic processes. Typical catalytic processes of highest industrial relevance are, for example, fluidized catalytic cracking,[3,4] hydroxylation of phenol,[5] and hydration of cyclohexene to cyclohexanol.[6] The main drawback of nanosized zeolites is their tendency to agglomerate in solutions (typically aqueous). The tendency is due to the nanoparticles' high specific surfaces. To avoid agglomeration, which can cause blockage of the pore entrances, zeolitic nanoparticles can be stabilized by the deposition onto or incorporation into a mesoporous matrix (preparation of a microporous/mesoporous composite).[7−16] Efficient incorporation of zeolitic nanoparticles into/onto mesoporous matrices requires the preparation of zeolitic precursors with the particle size of up to 5 nm.

A successful preparation of above-described nanosized zeolites requires detailed knowledge of the zeolite crystallization process. However, although studied for more than a decade already, this process is still not well understood, and it also seems that there is no general mechanism that could be attributed to the formation of all zeolite topologies. Several groups investigated the growth mechanism of several different zeolitic systems using various methods. The silicate precursors for the formation of colloidal silicalite-1 particles in the presence of TPAOH were studied by cryo-TEM and DLS,[17−19] and by theoretical evaluation.[20] A profound investigation on crystallization mechanism of silicalite-1 using a number of complementary techniques such as ^{29}Si NMR, IR, XRD, SAXS, TEM, and N_2 sorption was performed by the group in Leuven and their co-workers,[21−25] and by Hsu et al.[26] Formation of LTA-type

Received: September 6, 2010
Revised: January 11, 2011
Published: February 10, 2011

nanoparticles from amorphous silica aggregates was investigated by Mintova et al.[27] A review of the formation mechanisms and applications concerning nanosized zeolites was published by Tosheva et al.[28]

There have been several studies also on the growth of zeolite-Beta, which is particularly interesting, because of its catalytic potential in hydrocarbon transformation reactions and in catalytic dewaxing of petroleum oils.[29,30] Growth of zeolite-Beta nanoparticles with different Si/Al ratios was investigated using DLS, XRD, TEM, ^{29}Si and ^{27}Al NMR, and IR.[31] The effect of fluoride ions on zeolite-Beta growth was studied by Jon et al.[32] The formation of zeolite-Beta containing different Si/Al ratios by the steam-assisted crystallization (SAC) process was studied by XRD, solid-state ^{29}Si NMR, and Raman spectroscopy.[33−35] Although a plausible crystallization mechanism was proposed, the description is not valid for the hydrothermal synthesis of zeolite-Beta from a colloidal solution. Very recently, a mechanism of aluminum-containing zeolite-Beta formation in dilute solutions was investigated by DLS, SAXS, and TEM.[36] When such solutions were heated, three populations of particles were detected: primary particles with dimensions of <3 nm, secondary particles with dimensions of 6−50 nm, and tertiary particles with dimensions of >200 nm. It was concluded that the tertiary particles are formed and evolve into zeolite-Beta crystals only in solutions containing aluminum.

In this work, we investigate the crystallization process of aluminum-free zeolite-Beta functionalized by titanium. Titanium-modified zeolite-Beta shows remarkable catalytic activity for the selective epoxidation of several alkanes[37−39] and for the cracking of polyolefins.[40] It also exhibits photocatalytic activity for the reduction of carbon dioxide.[41] A study of zeolite formation, together with the study of transition-metal incorporation is, at least to our knowledge, presented for the first time. The paper is organized in two parts. In the first one, we follow the formation of nanoparticles from oligomers and condensation of these particles into zeolitic crystallites by spectroscopic techniques. In this way, we provide a complementary view at a smaller (atomic) scale to the view provided by Hould and Lobo.[36] We also compare the mechanism of crystallization of aluminum-free zeolite-Beta with the recently updated description of mechanism of colloidal silicalite-1 crystallization,[24,25] and show that, in a rough view, a unified description for the crystallization of both all-silica types of zeolites is possible. The second part of the paper deals with the incorporation of small amounts of titanium into the silicate framework of zeolite-Beta. We employ X-ray absorption spectroscopy to explore the local surroundings of Ti atoms in the samples at various stages of the synthesis, and we show that these metal ions are incorporated into the growing silicate framework at a very early stage of the synthesis.

EXPERIMENTAL SECTION

Synthesis of Colloidal Ti-Beta. Colloidal zeolite Ti-Beta particles used for formation and growth investigations were synthesized by the procedure described previously by our group.[13] In this procedure, silicic acid is used as a source of silicon. We hoped that rather slow dissolution of this silica precursor would lead to slower formation and growth of zeolitic particles and would thus enable better control over the particle size in the Ti-Beta product.

The synthesis started with a dissolution of tetraethylorthotitanate (95% TEOTi, Aldrich) in tetraethylammonium hydroxide (35% TEAOH, Aldrich) and was followed by slow addition of silicic acid (99% SiO_2, Merck). After the particles of the silicic acid were dispersed, the obtained viscous gel with component molar ratios of 0.025 TiO_2: SiO_2: 0.55 TEAOH: 8.8 H_2O was transferred to 45-mL Teflon-lined stainless-steel autoclaves and hydrothermally treated at 403 K for different periods of time (0−72 h). Upon thermal treatment, the initial viscous gel transformed to a clear gel. Its pH value was equal to 12, and it did not change over the entire period of hydrothermal treatment.

In this article, we refer to the samples by the time they were hydrothermally treated, e.g. in the 1 h sample, the crystallization process was stopped after 1 h. More precisely, the autoclave with the initial gel was put in an oven that was already at a temperature of 403 K, and after 1 h, it was taken out of the oven and quickly cooled in water. In such a way, the termination of the hydrothermal treatment was abrupt, but the onset of the treatment at 403 K was not, because the autoclave and the initial gel did need some time to reach the required temperature. For gels that were treated only for a short period of time (e.g., 0.5 or 1 h), the time needed to reach 403 K thus might actually represent a substantial fraction of the entire time of the treatment. Nevertheless, even though it is difficult to specify the exact duration of hydrothermal treatment, the difference in the duration of this treatment for different samples is very well-defined.

Ti-Beta gels used for ^{29}Si NMR investigations were analyzed as obtained from autoclaves. Liquid gels were subsequently dried overnight under ambient conditions to obtain dry Ti-Beta gels used for solid-state NMR, XRD, FT-IR, and XAS analysis. Titanium content within all dried gels was constant (0.9 mol %).

Characterization. Liquid- and solid-state ^{29}Si NMR spectra were recorded on a 600 MHz (14.1 T) Varian VNMRS spectrometer, using a Varian 5-mm broadband liquids probe and a Varian 3.2-mm MAS solids probe, respectively. Solid samples were spun with the spinning rate of 10 kHz. Liquid- and solid-state NMR spectra were recorded using a single-pulse excitation, a repetition delay of 20 s (for liquids) or 50 s (for solids), and an accumulation number of 1200. Spectra were decomposed into individual contributions of Gaussian or Lorentzian shape by DMFIT program.[42] Quantitative character of liquid-state NMR spectra was ascertained by preparing all the samples from the same initial gel, by transferring these samples to identical NMR tubes, and by recording their liquid-state ^{29}Si NMR spectra on a single NMR probe under identical conditions (temperature, strength and duration of the radio frequency excitation pulse, duration of the repetition delay, etc.). Care was also taken that the repetition delay between consecutive scans was sufficiently long to allow ^{29}Si magnetization to relax.

Elemental analyses of selected products were performed by energy-dispersion X-ray analysis (EDAX) with an INCA Energy System (Oxford Instruments) attached to a Zeiss Supra 3VP field-emission gun scanning electron microscope (FEG-SEM).

Powder X-ray diffraction (XRD) patterns of the dried products were collected on a PANalytical X'Pert PRO high-resolution diffractometer with Alpha1 configuration, using Cu Kα radiation (1.5406 Å) in the range from 5° 2θ to 35° 2θ with a step of 0.034° per 100 s, using a fully opened X'Celerator detector.

HRTEM measurements were performed on a 200-kV field-emission gun (FEG) microscope (JEOL Model JEM 2100). Dried samples were dispersed in ethanol and placed on a copper grid. Grid was additionally evaporated with carbon to avoid excessive charging of the sample.

X-ray absorption spectra of the samples and reference compounds were measured in the energy region of the Ti K-edge

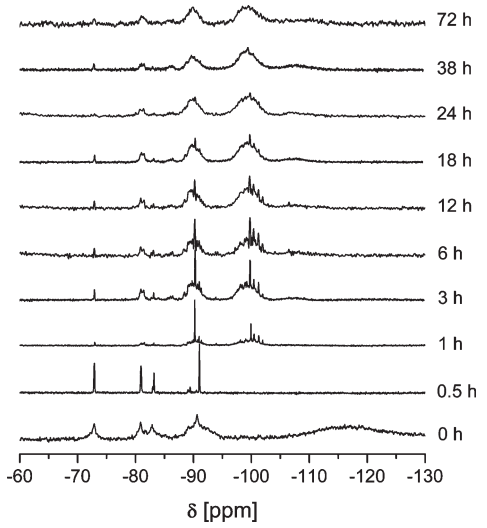

Figure 1. Liquid-state ^{29}Si NMR spectra of Ti-Beta gels. Crystallization times are listed on the right-hand side of the corresponding spectra.

in transmission detection mode at beamline C of HASYLAB synchrotron facility at DESY in Hamburg. A Si(111) double-crystal monochromator was used with the energy resolution of ~1 eV at the Ti K-edge (4966 eV). Higher harmonics were effectively eliminated by a slight detuning of the second monochromator crystal, keeping the intensity at 70% of the rocking curve with the beam stabilization feedback control. The intensity of the monochromatic X-ray beam was measured by three consecutive ionization chambers filled with 600 mbar N_2, 160 mbar Ar, and 220 mbar Ar for the first, second, and third ionization chamber, respectively. The dried gel samples were prepared as homogeneous self-supporting pellets with the total absorption thickness (μd) of ~2.5 above the Ti K-edge. The absorption spectra of the initial, 1 h, 6 h, and 28 h gels and of a final Ti-Beta product with a template still present in the pores were measured within the interval [−250 eV, 1000 eV], relative to the Ti K-edge. In the XANES region equidistant energy steps of 0.3 eV were used, while, for the EXAFS region, equidistant k-steps ($\Delta k \approx 0.03$ Å^{-1}) were adopted with the integration time of 1 s/step. Exact energy calibration was established with the simultaneous absorption measurements on Ti metal foil inserted between the second and third ionization cell.

RESULTS AND DISCUSSION

1. Formation of Zeolite-Beta Particles. To monitor the crystallization process of Ti-Beta zeolite, the synthesis of the zeolite was stopped at different times during hydrothermal treatment and the gels were subjected to liquid-state ^{29}Si NMR measurements. Afterward, the gels were dried and analyzed again using solid-state ^{29}Si NMR spectroscopy, XRD, and IR spectroscopy. The obtained liquid-state ^{29}Si NMR spectra are presented in Figure 1. Oligomerization of silicate species starts immediately after the preparation of the initial gel. In the spectrum of the 0.5 h sample, we can thus observe signals of silicon dimers resonating at −81.0 ppm, cyclic trimers resonating at −83.0 ppm and −83.2 ppm, as well as the rudiments of double three-membered rings resonating at −91.0 ppm. The signals were assigned to different silicon oligomers according to the literature.[25,43] A peak at −72.9 ppm, which corresponds to Si monomers (Q^0), is also present in the spectrum.

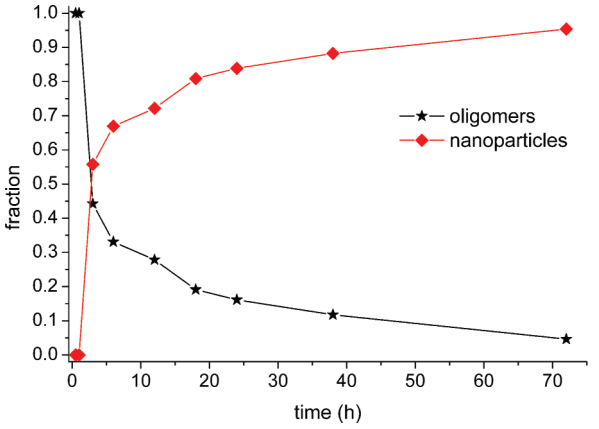

Figure 2. Abundance of Si oligomers and nanoparticles within Ti-Beta gels.

Simple building units start to connect into more-complex silicon oligomers after ~1 h of hydrothermal synthesis. Therefore, in the NMR spectrum of the 1 h sample, the peaks with chemical shifts of −90.3 ppm and −99.8 ppm become more pronounced. According to the literature,[44] these peaks can be ascribed to double three-membered rings and double four-membered rings, respectively. After ~3 h of hydrothermal treatment, a wide range of signals with different chemical shifts appear in the Si NMR spectrum, indicating the existence of a large variety of building units. The signals can be divided into four different regions. In the first region, peaks with chemical shifts from −80 ppm to −82 ppm represent Q^1 Si atoms; peaks in the range from −82 ppm to −90 ppm and from −90 ppm to −104 ppm are attributed to Q^2 and Q^3 Si atoms, respectively; and peaks with chemical shifts beyond −104 ppm belong to Q^4 Si atoms. With the symbol Q^n, we have denoted Si atoms that are through oxygen bridges connected to n other Si atoms.

The spectrum of the 3 h sample is composed of narrow signals as well as broad signals. This suggests that, after a few hours of hydrothermal treatment, individual oligomers start to connect or aggregate into bigger clusters: nanoparticles. The formation and growth of nanoparticles results in the broadening of the signals in the liquid-state NMR spectra, because such nanoparticles are much less mobile than the oligomers. The fractions of broad and narrow peaks in the spectra, which reflect the fractions of nanoparticles and the fractions of oligomers in the samples after different times of hydrothermal treatment, are plotted in Figure 2. We can see that, within the first six hours of the synthesis, the fraction of nanoparticles extremely quickly increases, at the expense of the fraction of oligomers. Afterward, the changes are slowed, and after 24 h of hydrothermal synthesis, the majority of oligomers already aggregate into nanoparticles and almost only broad signals are detected in the spectra of the 24 h, 38 h, and 72 h samples.

Interesting information about the nature of oligomers and nanoparticles can be obtained by analyzing their compositions, in terms of the relative fractions of the Q^n units (Figure 3). In oligomers, the Q^1 units, which are present at the very beginning of the synthesis, vanish very quickly and the dominant constituents become Q^2 and Q^3 units. During the first 24 h of synthesis, the fractions of these two types of units gradually change: the fraction of Q^3 units decreases and the fraction of Q^2 units increases. After that time, the Q^3/Q^2 ratio remains more or less constant. In the 72 h sample, the total amount of oligomers is negligibly small and the relative fractions of Q^2 and Q^3 units can no longer be determined.

dx.doi.org/10.1021/cm102547t |Chem. Mater. 2011, 23, 1337–1346

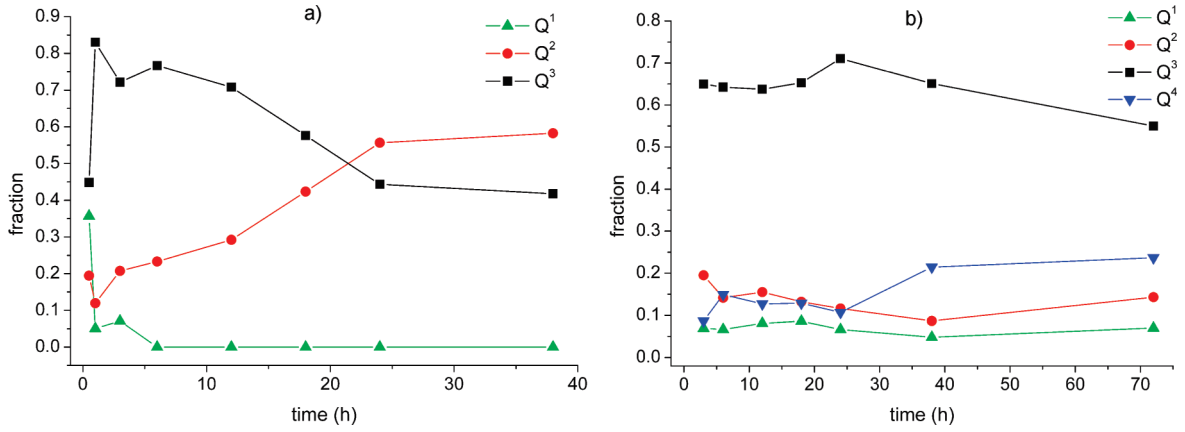

Figure 3. Relative fractions of Q^n species in (a) oligomers and (b) nanoparticles.

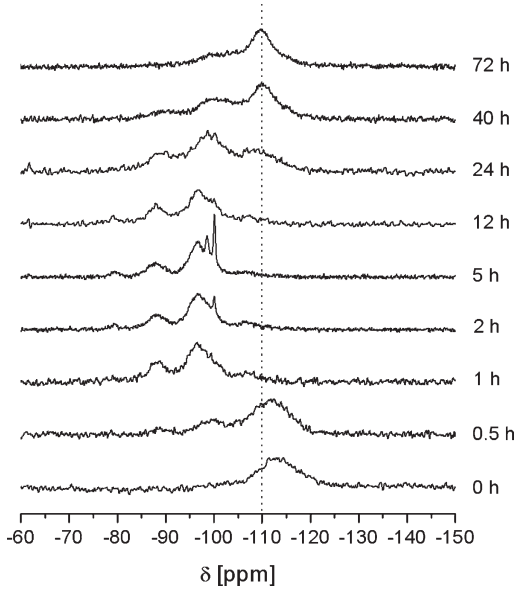

Figure 4. Solid-state ^{29}Si NMR spectra of dried Ti-Beta gels. The dotted vertical line at the center of the Q^4 Si peak at −110 ppm shows that this (Q^4) peak does not coincide with the peak belonging to the amorphous silicon.

The described evolution of the average composition of oligomers suggests that (i) only oligomers that are very rich in Q^3 units are used in the formation of nanoparticles, and (ii) the average fraction of Q^3 units decreases because the number of such "Q^3-rich" oligomers decreases. After 24 h of synthesis, almost all "Q^3-rich" oligomers, which are convenient for the formation of nanoparticles, are spent and only "Q^3-poor" oligomers with a Q^3/Q^2 ratio of ∼0.65 remain within the gel. These remaining oligomers are most probably less suitable for aggregation into nanoparticles; therefore, their concentration and composition remain approximately constant in the further course of the synthesis. A similar phenomenon was observed already during the formation of silicalite-1, where also some of the oligomers with a small Q^3/Q^2 ratio did not aggregate into nanoparticles.[24]

The changes in the composition of nanoparticles are less prominent than the changes in the composition of oligomers (Figure 3). We can see that, apart from slight deviations at the beginning of the synthesis, the composition of nanoparticles is practically constant during the first 24 h of thermal treatment. After that, the otherwise small concentration of Q^4 units slightly increases and the concentration of Q^3 units slightly decreases. These changes could be assigned to an increase of the size of the nanoparticles. As discussed by Aerts et al.,[24] if one assumes that nanoparticles are spherical and that they consist of a core that is composed of Q^4 Si species and a shell ∼0.3 nm thick that contains Q^3 species, one can use the Q^4/Q^3 ratio to estimate the size of nanoparticles. In our case, such an estimation shows that nanoparticles that are formed during the first 24 h have a diameter of ∼2 nm. The size of nanoparticles after longer periods of synthesis cannot be reliably estimated, because the increased Q^4/Q^3 ratio most probably corresponds to an average ratio for a mixture of nanoparticles with different sizes.

We would like to stress that the above estimation of the diameter of nanoparticles is rather rough, not only because of the assumptions about the particles' shape and about the core and shell composition, but also because we supposed that the broadening of the peaks in silicon NMR spectra stems only from reduced mobility and can thus only be assigned to nanoparticles. Aerts et al.[24] showed that the reason for line-broadening can also be a large distribution of slightly different chemical environments of oligomers. If that is the case, then the observed Q^4/Q^3 ratio of broad contributions does not accurately reflect the Q^4/Q^3 ratio of the nanoparticles and the above estimation of the diameter is inaccurate. However, the discrepancy between the observed Q^4/Q^3 ratio and the true ratio for the nanoparticles cannot be large; therefore, the diameter cannot deviate much from 2 nm.

The picture describing the formation of nanoparticles can be supplemented by solid-state NMR measurements. Silicon spectra recorded in dried gels obtained after different hydrothermal treatment times are presented in Figure 4. In the spectrum of the initial gel, only a broad signal at −113 ppm, which corresponds to the amorphous form of the silicon, is present. In the spectra of other samples, there are signals at −80 ppm, −88 ppm, −99 ppm, and −110 ppm, which can be assigned to Q^1, Q^2, Q^3, and Q^4 Si species, respectively. Apart from two minor exceptions, all these signals are broad and belong to nanoparticles obtained during the synthesis of zeolite-Beta. We can notice that, in the solid-state spectra of the 24, 40, or 72 h samples, the contributions of Q^4 Si species are much more pronounced than in the corresponding liquid-state spectra. There are two possible reasons for the difference between the solid-state spectra and the

liquid-state spectra. One is the drying procedure, which probably promotes condensation of the silicate framework and thus increases the relative fraction of Q^4 units within the dried samples. Another reason for weaker Q^4 signals in liquid-state spectra is in the fact that liquid-state NMR cannot detect particles with dimensions of several tens or even hundreds of nanometers. Indeed, quantitative comparison of the liquid-state NMR spectra for different samples shows that the total integrated intensity decreases with the duration of the synthesis. For example, the total integrated intensity of the 38 h spectrum is only ~60% of the intensity of the 1 h spectrum. The plot of the loss of intensity in liquid-state ^{29}Si NMR spectroscopy is shown in Figure 5. We can see that the major decrease in signal intensity occurs after 24 h of hydrothermal treatment. Such a loss of intensity tells us that, after 24 h, some bigger, liquid-state-NMR-invisible particles start to form in the gels. The inspection of Figure 5 allows us to roughly estimate the fraction of these bigger particles.

We expect that, in the solid-state NMR spectra, all nanoparticle populations are detected. During the first 24 h of synthesis, the composition of nanoparticles is almost constant (Figure 6). After that, the fraction of Q^4 species in dried gels starts to drastically increase, at the expense of the Q^3 species. Such an evolution of composition is clearly not the same as that observed for nanoparticles within gels, and this does speak in favor of the assumption that not only small nanoparticles with diameters of 2 nm but also bigger nanoparticles are detected by solid-state NMR. Both liquid- and solid-state NMR measurements suggest that (i) these bigger nanoparticles start to form after 24 h of synthesis and (ii) they are already very abundant after 38 h of the synthesis.

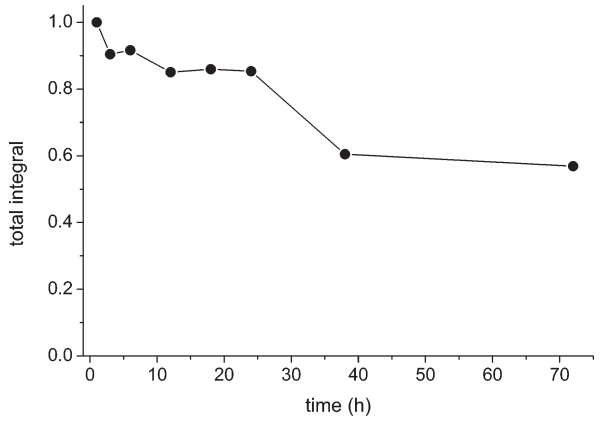

Figure 5. Total integrals of liquid-state ^{29}Si NMR spectra of Ti-Beta gels. The integrals were normalized with respect to the total integral of the spectrum of the 1 h sample.

The picture of the crystallization of zeolite-Beta that is based on the results of NMR measurements (i.e., quick formation of oligomers, agglomeration of oligomers into small nanoparticles, and subsequent formation of bigger nanoparticles) is consistent with the mechanism of formation of aluminum-containing zeolite-Beta proposed by Hould and Lobo.[36] The authors namely determined, using SAXS and DLS measurements, that the zeolite-Beta crystallization starts with a formation of primary particles with dimensions of <3 nm, followed by agglomeration of these particles into secondary particles with dimensions of 6−50 nm. Finally, they observed that the secondary particles condense into tertiary particles with dimensions of >200 nm. The time scales of zeolite-Beta formation in their case and our case are different; however, this is easily justified by the usage of different concentrations of initial gels and by the presence or absence of Al ions in the two synthesis approaches.

We can extend the comparison of our results to the results obtained by Hould and Lobo even further. Knowing that the 38 h gel consists of ~50% small nanoparticles and ~50% big nanoparticles, as learned from the missing liquid-state NMR intensity, and also knowing the composition of the small nanoparticles, we used the Q^4/Q^3 ratio determined from the solid-state NMR spectrum of the 40 h sample to estimate the size of the bigger/secondary nanoparticles. The estimated average diameter is ~8 nm and is again consistent with results of DLS measurements of Hould and Lobo (and with our own measurements; see the Supporting Information).

The secondary nanoparticles that are present in the gels after 38 h of synthesis already contain a very large fraction of Q^4 units, which suggests that they probably already have a zeolitic character and can act as seeds for the growth of zeolite-Beta crystallites. It is then expected that, if the concentration of the secondary particles is sufficient, tertiary particles (zeolite-Beta crystallites) will start to grow. The concentration of the secondary particles will increase with the hydrothermal treatment time and probably also by a drying procedure. Indeed, after 72 h of synthesis, the Q^4/Q^3 fraction of particles within the dried gel

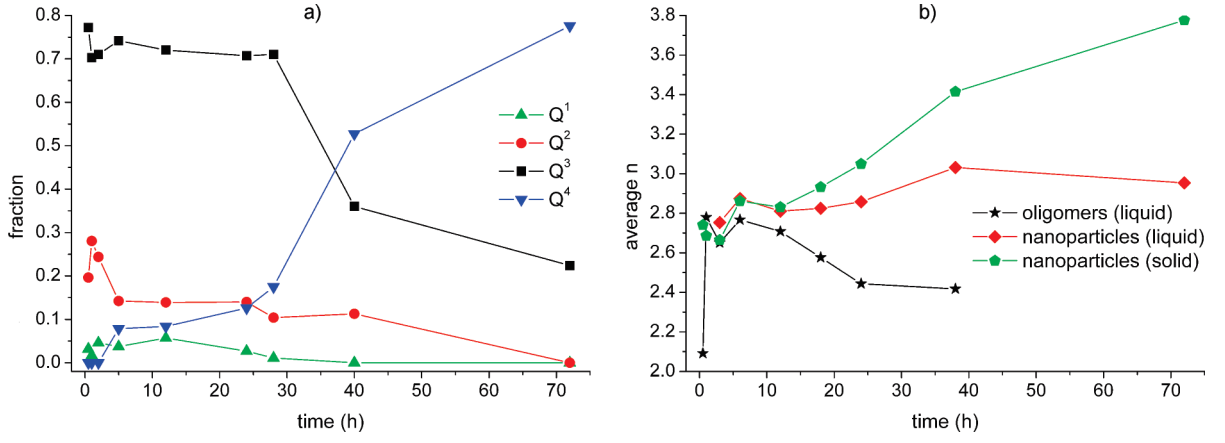

Figure 6. (a) Fractions of different silicon species (Q^n) in the dried gels, as a function of synthesis time, and (b) an average connectivity n of Si atoms in oligomers, primary nanoparticles, and in particles observed in dried gels.

dx.doi.org/10.1021/cm102547t |*Chem. Mater.* 2011, 23, 1337–1346

increases even further and reaches the value that is typical for the as-synthesized zeolite-Beta (obtained by the verified-synthesis procedure[45]). The average connectivity n at that time exceeds a value of 3.5 (see Figure 6).

It is interesting to compare the described observations with the observations on the crystallization of silicalite-1.[18−20,24−26] First of all, we note that the dynamics of nanoparticle formation from oligomers is different. In the case of silicalite-1, nanoparticles with a diameter of ∼2 nm are formed already before heating, immediately upon full hydrolysis of the silicon source (TEOS). After this initial step, no more small nanoparticles are formed during the synthesis of silicalite-1. The population of small nanoparticles consists of two types of particles with different degrees of condensation. Particles of only one type start to agglomerate into larger nanoparticles with a diameter of ∼6 nm, and these aggregate further into zeolitic crystallites. During the period of heating between 15 and 20 h, the formation of silicalite-1 crystallites becomes particularly rapid and induces a drastic increase in the pH value. In the case of zeolite-Beta, dissolution of the silicon source is slower and starts only upon heating of the initial viscous gel. The aggregation of oligomers into small nanoparticles is gradual and occurs over several hours. There is no steplike increase in the value of pH during the synthesis of zeolite-Beta, which also indicates that the formation of crystalline material from larger nanoparticles is not as rapid as it is in the case of silicalite-1. Otherwise, the formation of zeolite-Beta crystals undergoes the same steps as the formation of crystallites of silicalite-1: "Q^3-rich" oligomers (oligomers with a high Q^3/Q^2 ratio) form nanoparticles with typical dimensions of ∼2 nm; these nanoparticles aggregate into bigger nanoparticles with a diameter of ∼8 nm; when the concentration of the latter becomes sufficiently high, zeolitic crystallites start to grow via the addition of the nanoparticles. The mechanism of formation of zeolite-Beta is schematically summarized in Scheme 1.

Scheme 1. Formation of Zeolite-Beta (from Oligomers to Zeolitic Crystallites)[a]

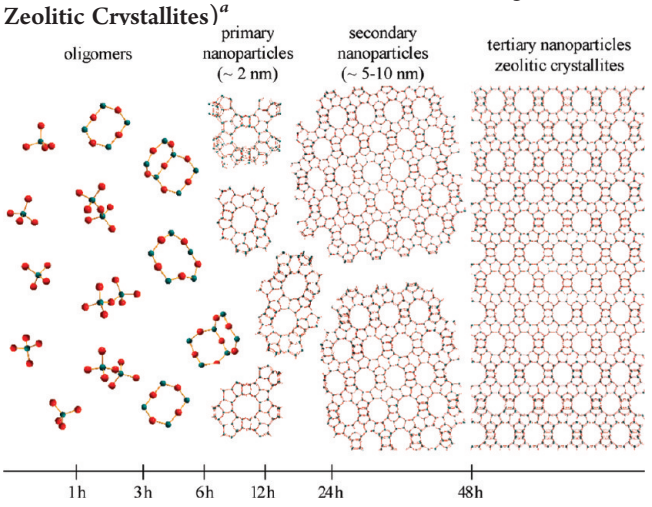

[a] Note that this is a schematic representation intended to give an appreciation about the average dimensions of primary and secondary nanoparticles, compared to the typical dimensions of a unit cell or of a 12-membered ring within zeolite-Beta. The typical dimensions listed in the scheme are average particle dimensions, and the nanoparticles in the gels are not as ordered or as uniform in size as presented in the scheme.

Results of NMR spectroscopy suggest that (i) after ∼24 h of zeolite-Beta synthesis, the first bigger/secondary nanoparticles are formed and (ii) at least some of these secondary nanoparticles already have a zeolitic character. This hypothesis can be verified also by some other techniques. The HRTEM image in Figure 7a shows nanoparticles with typical diameters of ∼5 nm in the dried product treated for 24 h. The diffraction rings in the selected-area electron-diffraction image shown in the inset of the figure prove the crystalline nature of the nanoparticles (diffraction rings instead of diffraction spots are obtained, because of the random orientation of several nanoparticles). Crystal lattices can be directly observed at higher magnifications (Figure 7b). Powder XRD of the dried gels hydrothermally treated for different periods of time (Figure 8) also unambiguously shows that the most-pronounced diffraction maximum of the zeolite-Beta phase at 22.4° 2θ first appears in the diffractogram of the product that was treated for 24 h. This means that, after 24 h of synthesis, ordered zeolite-Beta nanoparticles with dimensions above at least 5 nm must be present in the dried gel. With the increasing crystallization time, the degree of crystallinity of the product continuously increases and after 48 h, the product appears to be almost fully crystalline. Broad reflection with the peak at 7.67° 2θ indicates that zeolite-Beta crystallizes as a mixture of the A, B, and C polymorphs. (The zeolitic nature of the secondary

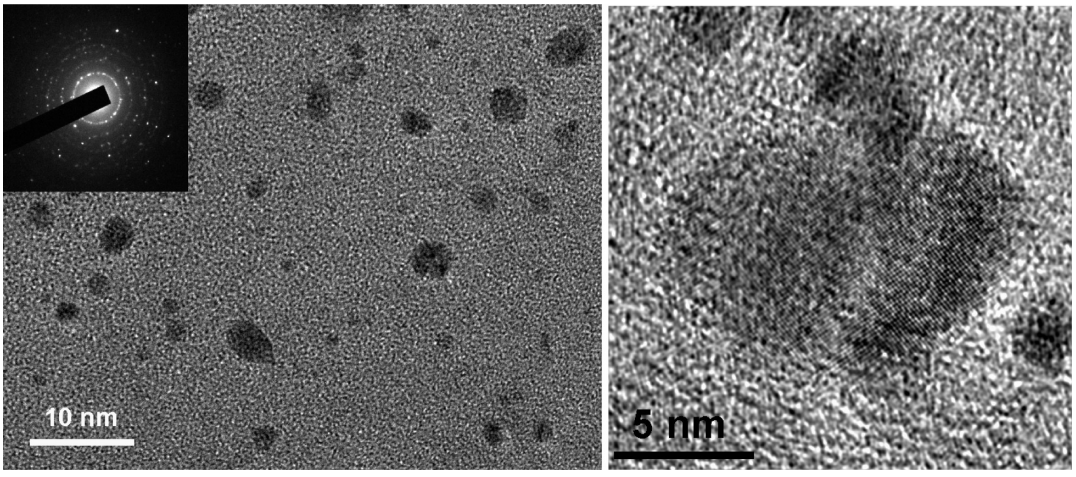

Figure 7. HRTEM images of (a) zeolite Ti-Beta nanocrystals obtained from a dried gel hydrothermally treated for 24 h. Inset in the upper left corner shows selected area diffraction pattern (SAED) of the corresponding particles. (b) Magnified image of the individual Ti-Beta nanoparticle, revealing its crystal lattice (magnification = 500 000).

nanoparticles is suggested also by FTIR spectroscopy; see the Supporting Information.)

2. Incorporation of Ti into Zeolite-Beta Particles. To study the incorporation of Ti atoms in the framework of zeolite-Beta, we used X-ray absorption spectroscopy. Information on the valence state and coordination of Ti atoms was obtained by X-ray absorption near-edge structure (XANES) analysis. The energy position of the Ti K absorption edge is shifted to higher energies as the oxidation state of the investigated atoms increases.[46,47] By comparing the Ti K-edge position of our samples to the edge positions of TiO_2 rutile, TiO_2 anatase, and as-synthesized titanium silicalite-1 reference compounds, as well as to the reference spectra measured on different Ti^{4+} oxides[48,49] (Figure 9a), we determined the valence state to be 4+ for all our samples. The position, shape, and intensity of the pre-edge resonance can also give us information about the coordination of Ti atoms.[48] In octahedrally coordinated Ti, such as that in rutile or anatase, three low-intensity pre-edge resonances are detected.[48,49] Tetrahedrally coordinated titanium, lacking a center of inversion, gives rise to a single high-intensity pre-edge peak.[48−50] Similarly, 5-fold coordinated Ti atoms exhibit a single strong pre-edge resonance, which is shifted ∼1 eV to higher energies, with respect to the pre-edge resonance of the 4-fold coordinated Ti.[48,49] Even the mixtures of above-mentioned coordinations can be determined from the intensity and position of pre-edge resonances, as was reported by Farges et al.[48]

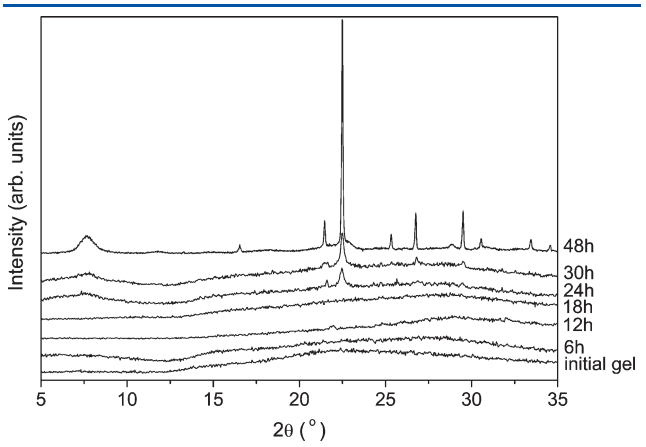

Figure 8. XRD diffractograms of the dried initial reaction gel and dried gels hydrothermally treated for specified times.

The XANES spectra of all our samples exhibit single pre-edge peaks, which are positioned at 4970 eV and have 30% of the intensity of the edge jump. Lower pre-edge peak intensities at the observed energy can be an indicator of a mixture of 4-fold coordinated framework titanium and octahedral extra-framework Ti, as suggested by Bordiga et al.[51] However, it has been shown that a similar decrease in the pre-edge peak intensity in microporous and mesoporous Ti silicates, such as Ti-Beta,[52,53] TiS-1,[54,55] and Ti-MCM-41,[56] more likely occurs because of the disorder and higher coordination numbers caused by water molecules or OH groups bonded (coordinated) to Ti atoms. It was reported that, when those samples were dehydrated, the pre-edge peak intensities increased to the values characteristic for tetrahedrally coordinated Ti atoms.[53,56]

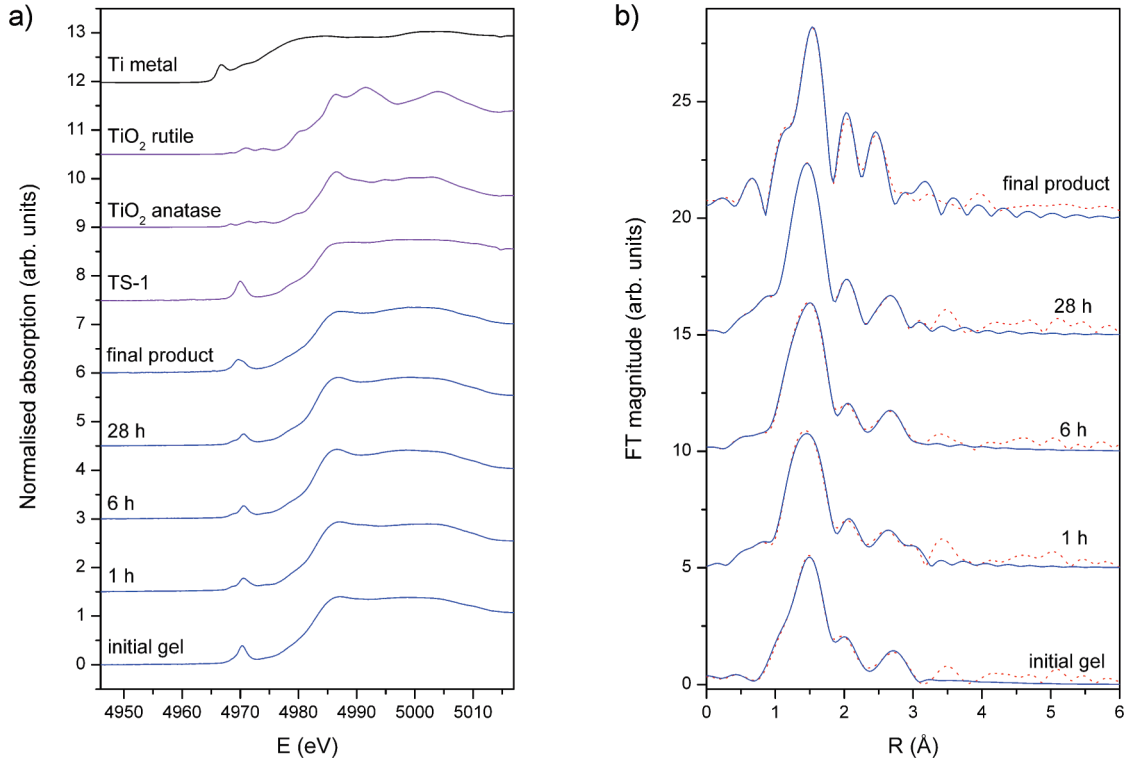

Figure 9. Results of X-ray absorption spectroscopy on Ti-Beta samples: (a) normalized Ti K-edge XANES spectra of the Ti-Beta gels, the Ti-Beta final product, and the Ti reference samples (Ti metal, TiO_2 rutile, TiO_2 anatase and as-synthesized TS-1). (b) Fourier transform magnitude of the k^3-weighted Ti EXAFS spectra, calculated in the k-range of 3.0−12.5 $Å^{-1}$ for Ti-Beta gels and 3.7−12.3 $Å^{-1}$ for the Ti-Beta final product. Dotted lines represent experimental curves and solid lines represent the best-fit EXAFS models.

dx.doi.org/10.1021/cm102547t |*Chem. Mater.* 2011, 23, 1337–1346

Table 1. Structural Parameters of the Nearest Coordination Shells around Ti Atom in the Ti-Beta Samples[a]

type of neighboring atom	average number, N	distance, R (Å)	Debye−Waller factor, σ^2 (Å^2)
	Ti-Beta Initial Gel		
O	3.8(4)	1.905(5)	0.009(1)
O	1.7(4)	2.49(2)	0.009(1)
O	2.4(1.0)	3.02(2)	0.009
Si	1	3.23(5)	0.010(5)
	Ti-Beta 1 h		
O	4.5(8)	1.897(7)	0.009(2)
O	1.3(7)	2.50(4)	0.009(2)
O	3(1)	3.01(2)	0.009
Si	1	3.37(5)	0.008(6)
	Ti-Beta 6 h		
O	5.1(6)	1.907(5)	0.009(1)
O	0.8(6)	2.51(5)	0.009(1)
O	6(2)	3.04(2)	0.011
Si	1	3.2(1)	0.015(9)
	Ti-Beta 28 h		
O	4.2(2)	1.891(2)	0.007(1)
O	1.3(2)	2.49(1)	0.007(1)
O	5(2)	2.89(2)	0.006(5)
Si	3(1)	2.92(2)	0.005(3)
	Ti-Beta Final Product		
O	2.8(4)	1.892(5)	0.002(1)
O	2.8(5)	2.427(9)	0.002(1)
Si	4	2.95(2)	0.012(2)
O	4	3.38(2)	0.006(3)

[a] Uncertainties in the last digit are given in parentheses.

More information on the local environment of Ti atoms in the samples was obtained by extended X-ray absorption fine structure (EXAFS) analysis. The Ti K-edge spectra of the samples were quantitatively analyzed with the IFEFFIT program packages,[57] using FEFF6 program code.[58] The best fit of the measured spectra provided coordination numbers, distances, and Debye−Waller factors of the nearest coordination shells. The Fourier transform of k^3-weighted Ti EXAFS spectra, together with the best-fit EXAFS model of the initial Ti-Beta gel, as well as the 1 h, 6 h, and 28 h gels and the Ti-Beta final product are presented in Figure 9b. The spectra were analyzed in the k-range of 3.0−12.5 Å^{-1} for Ti-Beta gels and 3.7−12.3 Å^{-1} for the Ti-Beta final product. The best fits for the spectra were found in the R-ranges from 1.1 Å to 3.3 Å for the gels and from 1.1 Å to 3.5 Å for the final product. The amplitude reduction factor (S_0^2 = 0.85) was determined on TiO_2 anatase and was kept fixed during the fit. A complete list of best fit parameters is given in Table 1.

For the Ti-Beta final product, we constructed the EXAFS model from the XRD data of actual zeolite-Beta structure, but allowed distortion of the oxygen coordination shell around Ti by introducing two different Ti−O distances. The analysis revealed 2.8 O atoms at a distance of 1.89 Å and 2.8 O atoms at a larger distance of 2.43 Å. In the second coordination sphere, the numbers of Si and O atoms were fixed at four, in accordance with the model, and the distances to the Ti atom obtained by fitting are 2.95 and 3.38 Å, respectively. Taking into account that no Ti atoms could be found in the second shell, we can conclude that all Ti atoms in the sample are (intra)framework and coordinated with one or two additional OH groups or H_2O molecules.

For Ti-Beta gels, five O atoms were found in the first coordination sphere: four at a shorter distance of 1.9 Å and the fifth at a distance of 2.5 Å. In the second coordination shell, O and Si atoms were found. Because of high correlations between parameters of the second coordination sphere, some of the Debye−Waller factors and coordination numbers for the second shell of the O and Si atoms were kept fixed during the fit. The 5-fold coordination of Ti atoms in the gels, along with the two different distances of O neighbors in the first coordination shell, indicate coordination of OH groups or water molecules to framework Ti. This is in good agreement with XANES results. Based on the number of O atoms in the first coordination shell and the Ti−O distances, we can exclude the presence of extra-framework TiO_2, in which Ti is octahedrally coordinated with six O atoms. We also found no Ti atoms in the second coordination sphere, which further excludes the presence of titanium oxides in Ti-Beta gels.

The analysis of EXAFS spectra shows similar Ti environments for shorter and longer hydrothermal treatment times. In the second coordination shell, we found silicon in all the samples, which means that Ti is coordinated to the forming silicate framework from the very beginning of the synthesis. In the initial gel and even after 1 h of hydrothermal treatment, Si is positioned at a greater distance from Ti (3.3 Å) than in the final product. After 6 h of synthesis, we can detect some changes and higher disorder in the second coordination shell. The Debye−Waller factors become larger and the number of O atoms found at a distance of 3 Å increases. These changes coincide with the period of the most rapid formation of primary nanoparticles from oligomers as detected by ^{29}Si NMR. After 28 h of hydrothermal sample treatment, the Ti−Si distance shortens to 2.92 Å, which is equal to the value found in the template-containing crystalline Ti-Beta. The number of Si atoms also draws nearer to four, as found in the final product. Here, the EXAFS data are in good agreement with the NMR, IR, and XRD analyses and show that, after approximately one day of synthesis, the sample already exhibits the same character as the final, fully crystalline Ti-Beta zeolite.

CONCLUSIONS

Liquid- and solid-state NMR enabled us to gain an atomic-scale-resolution insight into formation of zeolite-Beta. With this spectroscopic technique, we were able to distinguish the signals of oligomers, as well as those of small and big nanoparticles. More importantly, in all three types of species, we were able to determine the composition of the silicate framework, in terms of the distribution of Q^n units. When considering nanoparticles, the Q^3/Q^4 ratio enabled us to roughly estimate the dimensions of the particles and therefore compare the latter to the values obtained by other researchers by other techniques (e.g., by SAXS and DLS[36]).

Our measurements show that the synthesis of zeolite-Beta starts with a quick formation of oligomers, which then gradually aggregate into nanoparticles with an average diameter of 2 nm.

The nanoparticles are formed mostly (or at least much faster and efficiently) from oligomers with a high fraction of Q^3 units (oligomers with Q^3/Q^2 fraction larger than 4). After ~24 h of hydrothermal treatment, small nanoparticles begin to agglomerate into large nanoparticles with a diameter of ~8 nm. The fraction of Q^4 units within large nanoparticles is very high, ~50%, which indicates that at least some of these particles already have zeolitic character. The zeolitic character of the large nanoparticles is unambiguously confirmed by X-ray diffraction and electron diffraction. When the concentration of large nanoparticles becomes sufficiently high, their addition leads to the formation of zeolitic crystallites.

Crystallization of zeolite-Beta through the formation of small/primary nanoparticles, large/secondary nanoparticles, and zeolitic crystallites/tertiary particles agrees well with the observations of Hould and Lobo,[36] who prepared zeolite-Beta from very diluted solutions containing aluminum. The formation of similar species was also observed in the crystallization of silicalite-1.[18−20,24] Although time evolution in the formation of aluminum-free zeolite-Beta and silicalite-1 was different (gradual changes in the case of zeolite-Beta and stepwise changes in the case of silicalite-1), the measurements of Schoeman,[18,20] Aerts et al.,[24] and Hould and Lobo,[36] as well as our own measurements, indicate that the crystallization of both types of zeolites follows a very similar mechanism.

Studies of formation of the silicate framework were complemented with XANES and EXAFS investigations providing information on the incorporation of Ti into zeolite-Beta. The results show that, in the initial gel, Ti atoms form complexes with silicon oligomers, which then slowly become included in the growing zeolite structure as the primary and secondary nanoparticles are formed. After 28 h of synthesis, Ti appears to be incorporated in the framework in the same way as that in the final Ti-Beta product.

An important goal of this investigation was to learn how to prepare an efficient catalyst. Optimal catalytical activity of Ti-modified silicates is expected for particles with a zeolitic character and a surface contribution that is as large as possible. Our investigation of zeolite-Beta formation and growth suggests that this optimum can be achieved after ~24−30 h of crystallization, using the described hydrothermal conditions. Much shorter crystallization times (few hours) result in the formation of oligomer species and primary nanoparticles that are only partially condensed and do not have zeolitic character yet. When crystallization is longer (48 h or more), secondary nanoparticles, already possessing zeolitic character, tend to agglomerate into zeolite crystallites, which not only have a lower surface/volume ratio, but are also too big for potential incorporation into mesoporous matrices.

■ ASSOCIATED CONTENT

Supporting Information. Decomposition of selected liquid-state NMR spectra, particle-size distributions as obtained from the DLS measurements, large HRTEM images, results of FTIR spectroscopy, and UV−vis spectrum of the 72 h sample. This information is available free of charge via the Internet at http://pubs.acs.org/.

■ AUTHOR INFORMATION

Corresponding Author

*E-mail address: gregor.mali@ki.si.

■ ACKNOWLEDGMENT

This work was supported by the Slovenian Research Agency (Research Program P1-0021), and by DESY and the European Community's Seventh Framework Programme (FP7/2007-2013) ELISA (European Light Sources Activities), under Grant Agreement No. 226716. Access to synchrotron radiation facilities of HASYLAB (project II-20080058 EC) is acknowledged. We would like to thank Edmund Welter of HASYLAB for expert advice on beamline operation and Dr. Ksenija Kogej and Simona Prelesnik from the Faculty of Chemistry and Chemical Technology, University of Ljubljana, for their help with DLS measurements.

■ REFERENCES

(1) Yamamura, M.; Chaki, C.; Wakatsuki, T.; Fujimoto, K. *Zeolites* **1994**, *14*, 643.
(2) Schmidt, I.; Madsen, C.; Jacobsen, C. J. H. *Inorg. Chem.* **2000**, *39*, 2279.
(3) Rajagopalan, K.; Peters, A. W.; Edwards, G. C. *Appl. Catal* **1986**, *23*, 69.
(4) Camblor, M. A.; Corma, A.; Martínez, A.; Mocholí, F. A.; Perez-Pariente, J. *Appl. Catal.* **1989**, *55*, 65.
(5) van der Pol, A. J. H. P.; Verduyn, A. J.; van Hoff, J. H. C. *Appl. Catal* **1992**, *92*, 113.
(6) Camblor, M. A.; Corma, A.; Martínez, A.; Martínez-Soria, V.; Valencia, S. *J. Catal.* **1998**, *179*, 537.
(7) Čejka, J.; Mintova, S. *Catal. Rev. Sci. Eng.* **2007**, *49*, 457.
(8) Prokešová, P.; Petkov, N.; Čejka, J.; Mintova, S.; Bein, T. *Microporous Mesoporous Mater.* **2003**, *64*, 165.
(9) Mrak, M.; Novak Tušar, N.; Zabukovec Logar, N.; Mali, G.; Kljajić, A.; Arčon, I.; Launay, F.; Gedeon, A.; Kaučič, V. *Microporous Mesoporous Mater.* **2006**, *95*, 76.
(10) Mazaj, M.; Zabukovec Logar, N.; Mali, G.; Novak Tušar, N.; Arčon, I.; Ristić, A.; Rečnik, A.; Kaučič, V. *Microporous Mesoporous Mater.* **2007**, *99*, 3.
(11) van Oers, C. J.; Stevens, W. J. J.; Bruijn, E.; Mertens, M.; Lebedev, O. I.; van Tendeloo, G.; Meynen, V.; Cool, P. *Microporous Mesoporous Mater.* **2009**, *120*, 29.
(12) Meynen, V.; Cool, P.; Vansant, E. F.; Kortunov, P.; Grinberg, F. Karger, J.; Mertens, M.; Lebedev, O. I.; van Tendeloo, G. *Microporous Mesoporous Mater.* **2007**, *99*, 14.
(13) Mazaj, M.; Stevens, W. J. J.; Zabukovec Logar, N.; Ristić, A.; Novak Tušar, N.; Arčon, I.; Daneu, N.; Meynen, V.; Cool, P.; Vansant, E. F.; Kaučič, V. *Microporous Mesoporous Mater.* **2009**, *117*, 458.
(14) Choi, M.; Cho, H.; Srivastava, R.; Venkatesan, C.; Choi, D.; Ryoo, R. *Nat. Mater.* **2006**, *5*, 718.
(15) Srivastava, R.; Choi, M.; Ryoo, R. *Chem. Commun.* **2006**, 4489.
(16) Naik, S. P.; Chiang, A. S. T.; Thompson, R. W.; Huang, F. C.; Kao, H.-M. *Microporous Mesoporous Mater.* **2003**, *60*, 213.
(17) Schoeman, B. J. *Microporous Mater.* **1997**, *9*, 267.
(18) Schoeman, B. J. *Zeolites* **1997**, *18*, 97.
(19) Tsay, C. S.; Chiang, A. S. T. *Microporous Mesoporous Mater.* **1998**, *26*, 89.
(20) Schoeman, B. J. *Microporous Mesoporous Mater.* **1998**, *22*, 9.
(21) Ravishankar, R.; Kirschock, C.; Schoeman, B. J.; Vanoppen, P.; Grober, P. J.; Storck, S.; Maier, W. F.; Martens, J. A.; de Schryver, F. C.; Jacobs, P. A. *J. Phys. Chem. B* **1998**, *102*, 2633.
(22) Ravishankar, R.; Kirschock, C. E. A.; Knopps-Gerrits, P.-P.; Feijnen, E. J.; Grober, P. J.; Vanoppen, P.; de Schryver, F. C.; Miehe, G.; Fuess, H.; Schoeman, B. J.; Jacobs, P. A.; Martens, J. A. *J. Phys. Chem. B* **1999**, *103*, 4960.
(23) Kirschhock, C. E. A.; Kremer, S. P. B.; Grobet, P. J.; Jacobs, P. A.; Martens, J. A. *J. Phys. Chem. B* **2002**, *106*, 4897.
(24) Aerts, A.; Haouas, M.; Caremans, T. P.; Follens, L. R. A.; van Erp, T. S.; Taulelle, F.; Vermant, J.; Martens, J. A.; Kirschhock, C. E. A. *Chem.—Eur. J.* **2010**, *16*, 2764.

(25) Petry, D. P.; Haouas, M.; Wong, S. C. C.; Aerts, A.; Kirschhock, C. E. A.; Martens, J. A.; Gaskell, S. J.; Anderson, M. W.; Taulelle, F. *J. Phys. Chem. C* **2009**, *113*, 20827.
(26) Hsu, C.-Y.; Chiang, A. S. T.; Selvin, R.; Thompson, R. W. *J. Phys. Chem. B* **2005**, *109*, 18804.
(27) Mintova, S.; Olson, N. H.; Valtchev, V.; Bein, T. *Science* **1999**, *283*, 958.
(28) Tosheva, L.; Valtchev, V. *Chem. Mater.* **2005**, *17*, 2494.
(29) Borade, R. B.; Clearfield, A. *J. Phys. Chem.* **1992**, *96*, 6729.
(30) LaPierre, R. B.; Partridge, R. D.; Chen N. Y.; Wong, S. S. U.S. Patent 4 419 220, 1983.
(31) Mintova, S.; Valtchev, V.; Onfroy, T.; Marichal, C.; Közinger, H.; Bein, T. *Microporous Mesoporous Mater.* **2006**, *90*, 237.
(32) Jon, H.; Oumi, Y.; Itabashi, K.; Sano, T. *J. Cryst. Growth* **2007**, *307*, 177.
(33) Matsukata, M.; Osaki, T.; Ogura, M.; Kikuchi, E. *Microporous Mesoporous Mater.* **2002**, *56*, 1.
(34) Inagaki, S.; Nakatsuyama, K.; Saka, Y.; Kikuchi, E.; Kohara, S.; Matsukata, M. *Microporous Mesoporous Mater.* **2007**, *101*, 50.
(35) Inagaki, S.; Nakatsuyama, K.; Saka, Y.; Kikuchi, E.; Kohara, S.; Matsukata, M. *J. Phys. Chem. C* **2007**, *111*, 10285.
(36) Hould, N. D.; Lobo, R. F. *Chem. Mater.* **2008**, *20*, 5807.
(37) van der Waal, J. C.; Rigutto, M. S.; Van Bekkum, H. *Appl. Catal., A* **1998**, *167*, 331.
(38) Krijnen, S.; Sánchez, P.; Jakobs, B. T. F.; van Hooff, J. H. C. *Microporous Mesoporous Mater.* **1999**, *31*, 163.
(39) Renzo, F. D.; Gomez, S.; Teissier, R.; Fajula, F. *Stud. Surf. Sci. Catal.* **2000**, *130B*, 1631.
(40) Aguado, J.; Serrano, D. P.; Escola, J. M.; Garagorri, E.; Fernandéz, J. A. *Polym. Degrad. Stab.* **2000**, *69*, 11.
(41) Ikeue, K.; Yamashita, H.; Takewaki, T.; Davis, M. E.; Anpo, M. *J. Synch. Rad.* **2001**, *8*, 602.
(42) Massiot, D.; Fayon, F.; Capron, M.; King, I.; Le Calvé, S.; Alonso, B.; Durand, J. O.; Bujoli, B.; Gan, Z.; Hoatson, G. *Magn. Reson. Chem.* **2002**, *40*, 70.
(43) Haouas, M.; Taulelle, F. *J. Phys. Chem B* **2006**, *110*, 3007.
(44) Engelhardt, G.; Michel, D. *High-Resolution Solid-State NMR of Silicates and Zeolites*; John Wiley & Sons Ltd.: Chichester, U.K., 1987.
(45) Robson, H. *Verified Syntheses of Zeolitic Materials*; Elsevier Science B.V.: Amsterdam, 2001.
(46) Wong, J.; Lytle, F. W.; Messmer, R. P.; Maylotte, D. H. *Phys. Rev. B* **1984**, *30*, 5596.
(47) Arčon, I.; Mirtič, B.; Kodre, A. *J. Am. Ceram. Soc.* **1998**, *81*, 222.
(48) Farges, F.; Brown, G. E.; Rehr, J. J. *Phys. Rev. B* **1997**, *56*, 1809.
(49) Greegor, R. B.; Lytle, F. W.; Sandstrom, D. R.; Wong, J.; Schultz, P. *J. Non-Cryst. Solids* **1983**, *55*, 27.
(50) Waychunas, G. A. *Am. Mineral.* **1987**, *72*, 89.
(51) Bordiga, S.; Coluccia, S.; Lamberti, C.; Marchese, L.; Zecchina, A.; Boscherini, F.; Buffa, F.; Genoni, F.; Leofanti, G.; Petrini, G.; Vlaic, G. *J. Phys. Chem.* **1994**, *98*, 4125.
(52) Blasco, T.; Camblor, M. A.; Corma, A.; Pérez-Pariente, J. *J. Am. Chem. Soc.* **1993**, *115*, 11806.
(53) Blasco, T.; Camblor, M. A.; Corma, A.; Esteve, P.; Guil, J. M.; Martínez, A.; Perdigón-Melón, J. A.; Valencia, S. *J. Phys. Chem. B* **1998**, *102*, 75.
(54) Lopez, A.; Tuilier, M. H.; Guth, J. L.; Delmontte, L.; Popa, J. M. *J. Solid State Chem.* **1993**, *102*, 480.
(55) Bordiga, S.; Boscherini, F.; Coluccia, S.; Genoni, F.; Lamberti, C.; Leofanti, G.; Marchese, L.; Petrini, G.; Vlaic, G.; Zecchina, A. *Catal. Lett.* **1994**, *26*, 195.
(56) Blasco, T.; Corma, A.; Navarro, M. T.; Pérez-Pariente, J. *J. Catal.* **1995**, *156*, 65.
(57) Ravel, B.; Newville, M. J. *J. Synchrotron Rad.* **2005**, *12*, 537.
(58) Rehr, J. J.; Albers, R. C.; Zabinsky, S. I. *Phys. Rev. Lett.* **1992**, *69*, 3397.